PCCP

Investigating the Li+ substructure and ionic transport in Li10GeP2−xSbxS12 (0 ≤ x ≤ 0.25)

Journal:	*Physical Chemistry Chemical Physics*
Manuscript ID	CP-ART-10-2022-004710.R1
Article Type:	Paper
Date Submitted by the Author:	27-Nov-2022

Complete List of Authors:	Helm, Bianca; University of Münster Gronych, Lara M.; University of Münster Banik, Ananya; WWU, Instituts für Anorganische und Analytische Chemie Lange, Martin; University of Münster Li, Cheng; Oak Ridge National Laboratory, Materials; Imperial College London, Zeier, Wolfgang; University of Muenster, Institute of Inorganic and Analytical Chemistry

ARTICLE

Investigating the Li^+ substructure and ionic transport in $Li_{10}GeP_{2-x}Sb_xS_{12}$ ($0 \leq x \leq 0.25$)

Received 00th January 20xx,
Accepted 00th January 20xx

DOI: 10.1039/x0xx00000x

Bianca Helm,[a] Lara M. Gronych,[a] Ananya Banik,[a] Martin A. Lange,[a] Cheng Li,[b] and Wolfgang G. Zeier,*[a,c]

Understanding the correlation between ionic motion and crystal structure is crucial for improving solid electrolyte conductivities. Several substitutions in the $Li_{10}GeP_2S_{12}$ structure have been shown favorable impact on the ionic conductivity, amongst others Sb(+V) in $Li_{10}GeP_2S_{12}$. However, here the interplay between structure and ionic motion remains elusive. X-ray diffraction, high-resolution neutron diffraction, Raman spectroscopy and potentionstatic impedance spectroscopy are employed to explore the impact of Sb(+V) on the $Li_{10}GeP_2S_{12}$ structure. The introduction of antimony elongates the unit cell in *c*-direction and increases the M(1)/P(1) and Li(2) polyhedral volume. Over the solid solution range, the Li^+ distribution remains similar, an inductive effect seems to be absent and the ionic conductivity is comparable for all compositions. An effect of introducing Sb(+V) in $Li_{10}GeP_2S_{12}$ cannot be corroborated.

Introduction

The search for superb solid ionic conductors ($\sigma_{RT} > 10$ mS·cm^{-1}) to replace liquid electrolytes in Li ion batteries and establish all-solid-state batteries is on-going.[1–3] Solid electrolytes reduce the combustion risk and enhance the rigidity of the batteries.[1,3,4] Within the last years, many researchers focused on sulfide-based conductors, e.g. argyrodite Li_6PS_5X (X = Cl, Br, I),[5–8] thio-LISICON $Li_xM_{1-y}M'_yS_4$ (M = Ge, Si, and M' = P, Sb, Al, Ga),[9–12] and the $Li_{10}GeP_2S_{12}$ (LGPS) family,[13–17] using substitutions to understand the underlying Li ion diffusion mechanism.

Especially, LGPS was heavily investigated due to its initial high room-temperature ionic conductivity of 12 mS·cm^{-1}.[13] This fast Li^+ motion is possible due to the LGPS structure type (Figure 1). The sulfur anions form a distorted body-centered cubic lattice which is thought to be the most beneficial for easy ion migration.[18] LGPS has two crystallographic sites for central cations, M(1)/P(1) and P(2) which are either occupied by germanium and phosphorus $(M/PS_4)^{n-}$ (Wyckoff 4*d*) or only phosphorus $(PS_4)^{3-}$ (Wyckoff 2*b*), respectively (Figure 1a).[13] The M(1)/P(1) site is edge-sharing to the octahedral Li(2) site (Wyckoff 4*d*) forming a chain along the *c*-direction (Figure 1a). The tetrahedral Li(4) site shares an edge with P(2) tetrahedron and both sites are corner-sharing to the octahedral Li(2) site. The Li(1) (Wyckoff 16*h*) and Li(3) (Wyckoff 16*h*) sites, being edge- and corner-sharing with the M(1)/P(1) and P(2) site, form a "diffusion tunnel" along the *c*-direction, which is the main one-dimensional diffusion pathway in LGPS (Figure 1b and 1c).[13,19]

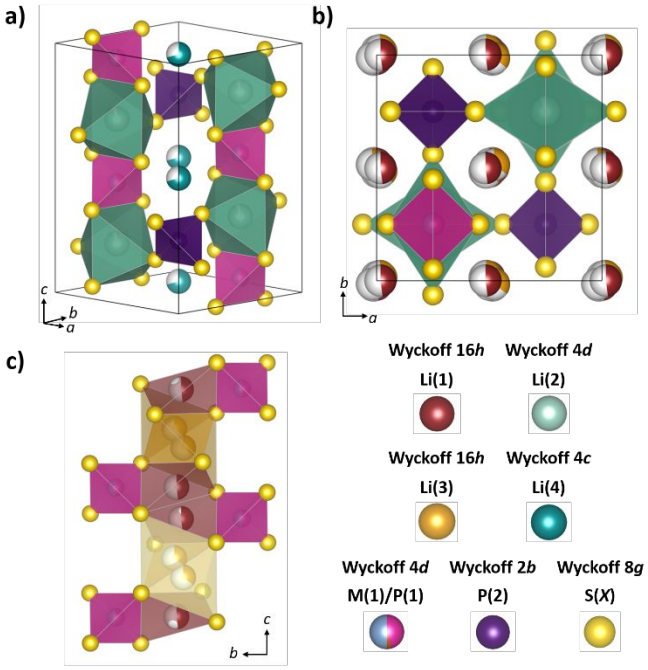

Figure 1: *(a) Visualization of the framework of LGPS. The M(1)/P(1) tetrahedra form a channel along the c-direction in combination with the Li(2) octahedra. The tetrahedral Li(4) position shares an edge to the P(2) tetrahedron and corners to Li(2) octahedron. Li(4) tetrahedron omitted for simplicity. (b) Top-down view on tunnel-like Li^+ diffusion pathways of Li(1) and*

[a] *Institute of Inorganic and Analytical Chemistry, University of Münster, Corrensstrasse 28/30, D-48149 Münster, Germany.*
[b] *Neutron Scattering Division, Oak Ridge National Laboratory (ORNL), 1 Bethel Valley Road, Oak Ridge, Tennessee 37831-6473, United States.*
[c] *Institute für Energie- und Klimaforschung (IEK), IEK-12: Helmholtz-Institut Münster, Forschungszentrum Jülich, 48149 Münster, Germany.*

Electronic Supplementary Information (ESI) available: [X-ray diffraction data and Neutron diffraction data with corresponding Rietveld refinements and structural tables; room-temperature and low temperature Crystallographic information files (CIF); Raman spectroscopy, additional information on Li^+ substructure, Arrhenius plots and pellet geometries]. See DOI: 10.1039/x0xx00000x

Li(3) from the ab-plane. (c) Polyhedral connectivity between the cation disordered site and the Li⁺ diffusion chain.

Additionally, Li(2) and Li(4) bridge the Li(1)-Li(3) tunnel in the *ab*-plane offering the possibility of three-dimensional diffusion in which the Li(1)-Li(4) pathway seems to be preferred over the Li(2)-Li(3) pathway.[20–23]

To date, several substitutions were performed within the LGPS family to study structural influences on conductivity, derive design principles, and further improve the conductivity. Higher conducting compositions of the Li-Sn-Si-P-S system showed three-dimensional diffusion pathways, while the lower conducting samples exhibited one-dimensional diffusion pathways indicated by maximum entropy method.[19] Furthermore, it was observed that the Li(1)-Li(1) distance shortened with higher temperatures and, corresponding higher conductivities, creating a Li(1) octahedron rather than having Li^+ located in the Li(1) tetrahedron.[19] Gao *et al*. found an increase in unit cell volume by co-substituting $Li_{10}SnP_2S_{12}$ with Sb and O, achieving the highest conductivity of 2.58 mS·cm^{-1} for $Li_{10}SnP_{1.84}Sb_{0.16}S_{11.6}O_{0.4}$.[24] The introduction of oxygen led to a blue shift of the $(SnS_4)^{4-}$ and $(PS_4)^{3-}$ vibrational energies, and an additional signal at 421 cm^{-1} in the Raman spectrum which is attributed to the $(SbS_4)^{3-}$ unit.[24] Wang *et al*. found that the solubility limit of antimony in the substitution series $Li_{10}SnP_{2-x}Sb_xS_{12}$ is x(Sb) = 0.2, and that the antimony substitution does not affect the vibrations of $(SnS_4)^{4-}$ and $(PS_4)^{3-}$ in the Raman spectra. However, the broadening of the unit cell has been suggested to be beneficial for ionic conductivity reaching a maximum of 2.43 mS·cm^{-1} for $Li_{10}SnP_{1.8}Sb_{0.2}S_{12}$.[25] Kato *et al.* investigated the $Li_{10}(Ge_{1-x}M_x)P_2S_{12}$ substitution series with M = Si and Sn finding that the conductivity is a function of the unit cell volume peaking at $Li_{10}GeP_2S_{12}$ and declining to $Li_{10}SiP_2S_{12}$ and $Li_{10}SnP_2S_{12}$.[26] Structural in-depth investigations of the substitution series $Li_{10}Ge_{1-x}Sn_xS_{12}$ by Krauskopf *et al.* revealed that a shortened S(3)-S(3) distance and an inductive effect are both detrimental to the conductivity.[27] A follow-up study on the inductive effect by Culver *et al.* showed that the substitution of Ge^{4+} with Sn^{4+} affects the bond strength and polarity, ultimately leading to a higher negative charge on the sulfur which in turn impedes Li^+ transport.[28] A schematic of this effect, how it is suggested to affect the $Li_{10}GeP_{2-x}Sb_xS_{12}$ substitution series based on the electronegativity difference of phosphorus and antimony, can be found in Figure 2. Liang *et al.* synthesized the substitution series $Li_{10}GeP_{2-x}Sb_xS_{12}$ and found that the solubility limit of antimony in the structure was x(Sb) = 0.25. The Sb^{5+} substitution increased the unit cell volume of LGPS and improved the conductivity up to 17.5 mS·cm^{-1}.[29]

The studies by Liang *et al*.[29] as well as Culver *et al.*[28] inspired this work to investigate the impact of Sb(+V) on the Li^+ substructure and to possibly detect an inductive effect in the substitution series $Li_{10}GeP_{2-x}Sb_xS_{12}$ ($0 \le x \le 0.25$). The introduction of Sb(+V) into the LGPS structure is expected to introduce two changes intrinsic to P(+V) and Sb(+V): **(1)** The smaller P(+V) (r = 0.17 Å)[30] is replaced by the bigger Sb(+V) (r = 0.50 Å)[31]. The widening of the unit cell seems to have a positive effect on the conductivity as shown by Liang *et al.*,[29] however it remains elusive how exactly the framework and the Li^+ sublattice is affected. **(2)** The magnitude of the electronegativity on the phosphorus sites may be weakened due to the introduction of the more electropositive antimony (EN(P) = 12.8 eV·e^{-1} *vs*. EN(Sb) = 11.2 eV·e^{-1}) (see Figure 2).[32] Along the reasoning by Culver *et al.* for an inductive effect, in comparison with phosphorus the more electropositive antimony should increase the electron density on the sulfur atom and thus, worsen the conductivity which would be contradictory to the result by Liang *et al*.[29]

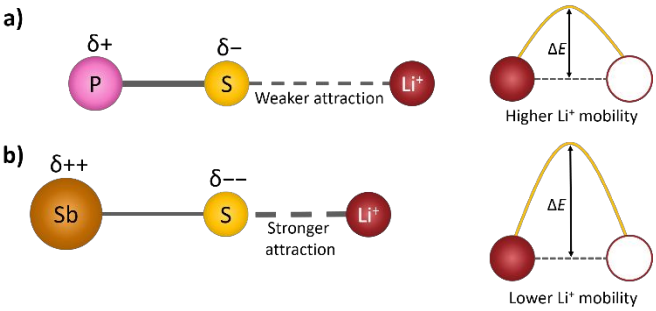

***Figure 2**: (a) Display on how the P-S bond affects the bypassing Li^+ ions. (b) Change in interaction between Li^+ ions and sulfur due to replacement of phosphorus by antimony. The interactions are based upon the electronegativities of each element and the effect cannot be corroborated in this work.*

In this work, by using a combination of X-ray and high-resolution neutron diffraction to detect structural changes, Raman spectroscopy to investigate changes in bond strength and impedance spectroscopy to determine the ionic conductivity we explore the substitution series $Li_{10}GeP_{2-x}Sb_xS_{12}$ ($0 \le x \le 0.25$). This work shows that introducing Sb(+V) into the structure elongates the unit cell in the *c*-direction and leads to an increase in the M(1)/P(1) as well as Li(2) polyhedral volume. Interestingly, all the Li ions distribute similarly over the four Li^+ sites showing no increase in Li^+ disorder and no influence of the change in electronegativity can be found, showing that (contrary to recent reports) the conductivity does not change and remains comparably high for all compositions.

Experimental Section

Synthesis. All synthesis steps were carried out under argon atmosphere in a glovebox (H_2O < 0.1 ppm, O_2 < 0.1 ppm). The substitution series $Li_{10}GeP_{2-x}Sb_xS_{12}$ ($0 \le x \le 0.25$) was prepared via mechanochemical synthesis in a planetary ball mill based on the procedure reported by Krauskopf *et al*.[27] Li_2S (Alfa Aesar, 99.9%), GeS (Sigma Aldrich, 99.99%), S (Acros Organics, 99.999%), P_2S_5 (Sigma Aldrich, 99%) and Sb_2S_3 were used in stoichiometric ratios with an excess of three weight percent of sulfur. The mixture was homogenized and then, transferred into a ball mill cup containing ZrO_2 milling media (Ø = 5 mm) using a milling-media-to-powder ratio of 30:1. Afterwards, the samples were milled for 48 hours at 400 rpm alternating ten minutes of milling and fifteen minutes of cooling. During the milling time the ball mill cup was opened twice to homogenize the mixture

and scrape off stuck powder from the walls by hand. Then, the powders were pelletized and transferred into preheated ampoules with carbon coating (dried at 800°C for two hours, dynamic vacuum). Finally, the sealed ampoule was placed into a furnace and was annealed at 500°C for 20 hours. The ramping rate to reach 500°C was 17°C·h^{-1}. The samples cooled naturally and were hand-ground for further characterizations.

The precursor Sb_2S_3 used here, was synthesized via a solid-state reaction.[33] Sb (ChemPur, 99.999%) and S (Acros Organics, 99.999%) were mixed in stoichiometric ratios and pelletized. Directly after, the pellets were transferred into a dried ampoule (800°C for two hours, dynamic vacuum). The samples were first annealed at 650°C for twelve hours with a heating rate of 40°C·h^{-1} and were then cooled with 60°C·h^{-1} to room-temperature. Afterwards, the samples were hand-ground for further use.

Powder X-ray diffraction. X-ray diffraction measurements were recorded with a Stoe STADI P diffractometer in Debye-Scherrer geometry with a Dectris MYTHEN2 1K detector. The radiation source was Mo K_α (λ = 0.7093 Å) employing a Ge(111) monochromator. The diffraction data was collected within a Q-range of 0.53 Å^{-1} to 12.39 Å^{-1}. All samples were measured in sealed in borosilicate glass capillaries (Hilgenberg, Ø = 0.5 mm).

Neutron powder diffraction. Neutron powder diffraction data of $Li_{10}GeP_{2-x}Sb_xS_{12}$ ($0 \leq x \leq 0.25$) samples was collected at Oak Ridge spallation neutron source (SNS, Oak Ridge National Laboratory). The samples are not ^{7}Li enriched but contain lithium in the abundant isotope mixture. The PAC automatic sample changer at POWGEN diffractometer (BL-11A beamline) was used. The samples (~ 3 g) were placed into a cylindrical vanadium can (Ø = 8 mm) and sealed with a copper gasket under inert conditions to prevent air exposure during the measurement. The diffraction data was collected for three and a half hours per diffractogram in high-resolution mode with a center wavelength of 1.5 Å. The samples were measured at 75 K, 150 K, 225 K and 300 K.

Rietveld analysis. Rietveld refinements were carried out on absorption-corrected neutron diffraction data and X-ray diffractograms using the TOPAS-Academic V6 software package.[34] For the room-temperature data, co-refinements were performed using both data sets, while for low temperature data (≤ 225 K) just neutron diffraction data was refined. The structural data obtained from neutron refinements of $Li_{10}GeP_2S_{12}$ from Culver *et al*. were used as starting model.[28] A convolution of pseudo-Voigt and GSAS back-to-back exponential functions was used to fit the profile shape.[35] Initially the (1) background, (2) scale factors of main and side phases, (3) lattice parameter and (4) the peak shape were refined. Once a good profile fit was achieved, the (5) atomic coordinates, (6) occupancies and (7) isotropic thermal displacements parameters were refined. During the co-refinements, Sb was probed on both P sites (Wyckoff 4*d* and Wyckoff 2*b*), however, Sb just occupies the Wyckoff 4*d* site,[13,14,29] as shown in Figure 1. The coordinates and thermal displacement parameters of Sb(1) and P(1) were hence constrained to be the same and the total occupancy was constrained to 0.5 considering the Ge occupancy on this site. (Table S1). Furthermore, the Li coordinates, occupancies and thermal displacement parameters were refined globally from the neutron diffraction data, while the Sb/P-ratio was refined globally from the X-ray diffraction data. For the rest of the structural parameters both data sets were considered. The low temperature neutron diffraction refinements were fit with the obtained room-temperature structural model for each substitution level.

VESTA was used to determine the polyhedral volumes.[36] The following data plots display the obtained errors which correspond to the estimated standard deviation. Only the polyhedral volume uncertainties were calculated using the total differential of the octahedron, tetrahedron or trigonal bipyramid volume considering the S-S bond distances as polyhedral edges and the corresponding bond length uncertainties. For simplicity, the formula of a perfect octahedron, tetrahedron or trigonal bipyramid was used. The crystallographic information files (CIFs), structural tables, used constraints (Figure S2, Table S1 – S7) as well as the temperature dependent volume changes (Figure S8 – S11) are reported in the Supporting Information.

Potentiostatic electrochemical impedance spectroscopy (PEIS). AC impedance spectroscopy was used to measure the ionic conductivities. Approximately 200 mg of each sample was compacted isostatically in form of a cylindrical pellet at 4.35 kbar for 40 minutes. Subsequently, the pellets were sintered at 400°C for ten minutes to enhance contact between the grains. The resulting pellets had relative densities ranging from 74% - 80% (Table S9). Thereafter, a thin gold layer was sputtered on each pellet side for 300 s at a current of 30 mA. Before measurement, the pellets were contacted with aluminium current collectors and sealed in pouch bags. A SP300 impedance analyser (Biologic) was used to carry out the impedance analysis within a frequency range of 7 MHz to 100 mHz, applying an excitation voltage amplitude of 10 mV. The monitored temperature range was 233 K – 333 K and the sample was equilibrated for one hour at each temperature before measuring. The impedance spectra were evaluated with RelaxIS 3 software (rhd instruments). The data quality was assessed using a Kramer-Kronigs analysis to determine the reliable frequency ranges. From room-temperature to 60°C the high conductivities led to inductances. Therefore, these impedance spectra are neglected for the determination of the activation energy as an underestimation of the conductivity results. The uncertainties of the ionic conductivity and activation energy were calculated from fit and geometrical errors. The capacitances were calculated from the capacitances of constant phase elements according to the Brugs' formula.[37]

Raman spectroscopy. The Raman measurements were carried out on a SENTERRA II from Bruker. A green laser with a wavelength of 532 nm and an objective lense with 20-fold magnification were employed. On every sample three different spots were measured with a laser power of 2.5 mW, an integration time of 1000 s and four Co-additions. Each sample was fixed on a specimen slide with Kapton® tape to prevent air and moisture exposure.

Results

Immobile framework. The impact of the replacement of P(+V) by Sb(+V) in the LGPS structure is probed on room-temperature X-ray and neutron diffraction data in the substitution series $Li_{10}GeP_{2-x}Sb_xS_{12}$ (Figure S1). In some samples, small fractions of impurities are observed (Figure 3a). For the LGPS, the additional reflections are assigned to orthorhombic Li_7PS_6 being part of the Li_2S-P_2S_5-GeS_2 system and thus, a possible impurity.[15,38] For nominal compositions x(Sb) ≥ 0.15, a different additional reflection can be observed at Q = 2.30 Å^{-1} which cannot be assigned to any specific phase.

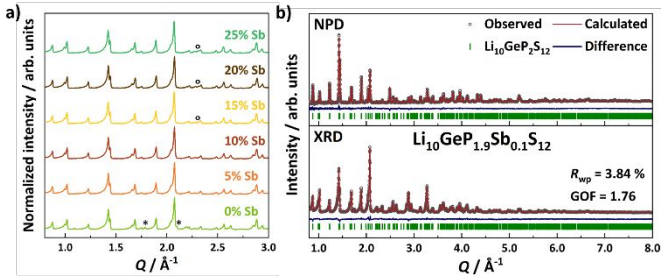

Figure 3: *(a) Overview of X-ray diffraction pattern of the substitution series $Li_{10}GeP_{2-x}Sb_xS_{12}$. The $Li_{10}GeP_2S_{12}$ sample shows Li_7PS_6 (Q = 1.78 Å^{-1} and 2.09 Å^{-1}) as an impurity. In addition, with higher substitution level, an unknown antimony side phase (Q = 2.30 Å^{-1}) forms. (Li_7PS_6 is marked with * and the unknown side phase is marked with °). (b) Exemplary Rietveld co-refinement for the nominal composition of $Li_{10}GeP_{1.9}Sb_{0.1}S_{12}$.*

Rietveld refinements against the room-temperature X-ray and neutron diffraction data are employed to reveal structural changes upon substitution. An exemplary co-refinement of neutron and X-ray diffraction data is shown in Figure 3b, the remaining refinement data as well as CIF files can be found in the Supporting information (Figure S2 and Table S1-S7). The refinement indicated that 7.65 ± 0.15 wt.-% of Li_7PS_6 is present in the LGPS sample. The unknown side phase developing in the compositions with x(Sb) ≥ 0.15 might be an antimony-related side phase considering the deviation from perfect solubility in the LGPS structure (Figure 4a). For comparison, Liang *et al.* synthesized the $Li_{10}GeP_{2-x}Sb_xS_{12}$ solution series in a similar fashion using different milling and annealing conditions, observing side phases, which differ from the here observed side phase, when x(Sb) exceeded 0.25.[29] Here, a smaller solubility limit for Sb is found in $Li_{10}GeP_{2-x}Sb_xS_{12}$. The following results are all shown against the refined antimony content to have a more realistic display of the changes in the structure than plots against the nominal antimony content can offer. The maximal substitution level is, as refined, 18 at.-% of antimony on the M(1)/P(1) site, whereas 12 at.-% antimony can be substituted on the M(1)/P(1) site before the side phase develops.

The lattice parameter a is not affected by the antimony substitution, while the lattice parameter c increases (Figure 4b). The tetragonal unit cell is elongated in c-direction, indicated by the increase in the c/a-ratio (Figure 4c). The tendency of symmetry reduction when substituting with antimony could be caused by the need of the structure to adjust the unit cell to the radii difference of 0.33 Å.[30,31] Herein, primarily the lattice parameter c is changed. The lattice parameters of the nominal composition $Li_{10}GeP_{1.85}Sb_{0.15}S_{12}$ agree well with the reported values by Liang *et al.*[29] Already published literature reports that the P(2) site (Wyckoff 2*b*) is only occupied by phosphorus, while the M(1)/P(1) site (Wyckoff 4*d*) shows cation disorder of P^{5+},Ge^{4+} and M^{n+} in LGPS.[13,14,29] Additionally, Liang *et al.* employed density functional theory calculations to determine the most stable position for antimony within the structure, concluding that antimony preferably occupies the M(1)/P(1) site.[29] The latter is observed in this study as well. The $(PS_4)^{3-}$ tetrahedron shows no volume changes, while the $(M/PS_4)^{n-}$ tetrahedron increases in volume since the smaller phosphorus ($r(P^{5+})$ = 0.17 Å)[30] is replaced by the bigger antimony ($r(Sb^{5+})$ = 0.50 Å)[31]. However, as indicated the overall structural changes are small in the order of maximum 2 %.

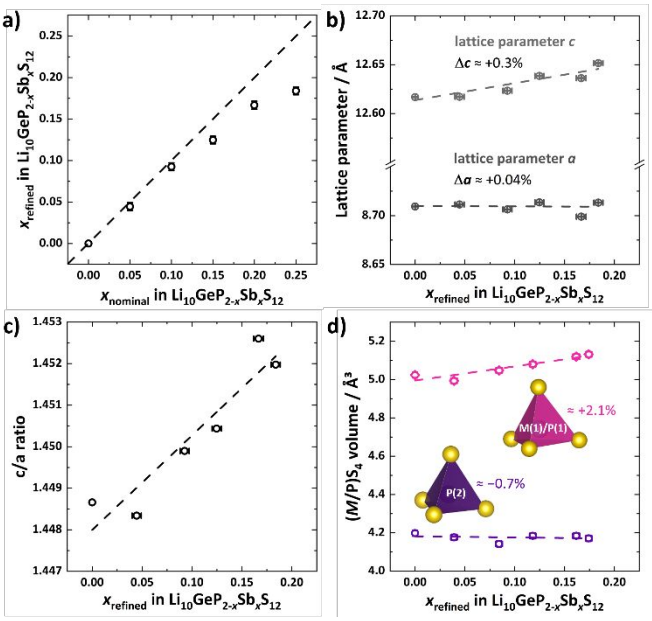

Figure 4: *(a) The nominal antimony content is plotted against the refined antimony content. At roughly 12 at.-% Sb on the P site, the refined antimony content starts to deviate from the nominal composition, indicating that the solubility has been reached. (b) The lattice parameter a is not changed (+0.04%) upon introduction of antimony, while lattice parameter c increases about 0.3%. (c) The c/a-ratio increases gradually with higher antimony content. (d) The P(2) tetrahedron volume decreases about 0.7% over the substitution series. The M(1)/P(1) tetrahedron increases about 2.1% with the introduction of Sb. The dashed lines represent guides-to-the-eyes and all structural changes are giving in percentage to gauge the minor overall changes.*

Furthermore, Raman spectroscopy was employed to detect changes in bond strength (Figure S3). The observed signals of the $(PS_4)^{3-}$ unit[39–41] $\nu_{symmetric}$ = 414 cm^{-1}, and $\nu_{deformation}$ = 278 cm^{-1}, and the signals of the $(GeS_4)^{4-}$ unit[28] $\nu_{symmetric}$ = 363 cm^{-1} are in good agreement with literature. At higher antimony contents, a shoulder develops at the symmetric

stretching mode of $(GeS_4)^{4-}$ at 387 cm^{-1} which may be related to the $(SbS_4)^{3-}$ unit. The reported Raman signals for the $(SbS_4)^{3-}$ symmetric vibrations range in between 360 cm^{-1} to 368 cm^{-1},[12,41,42] and for the asymmetric stretching mode at 389 cm^{-1} and 410 cm^{-1} or 421 cm^{-1}.[24,41,42] Thus, the occurring peak should be the asymmetric stretch of the $(SbS_4)^{3-}$ unit suggesting that the symmetric stretch of the $(SbS_4)^{3-}$ unit is hidden beneath the symmetric stretch of the $(GeS_4)^{4-}$ unit. To summarize, the Raman indicates that the bond strength of the $(PS_4)^{3-}$ unit is not influenced due to the similarity of the observed wavenumbers for every composition. In contrast to the work of Culver *et al*.[28] no direct changes to the bond strength along the series can be found. Wang *et al*. noticed likewise that antimony did not affect the $(SnS_4)^{4-}$ and $(PS_4)^{3-}$ vibration in the Raman spectrum for the substitution series $Li_{10}SnP_{2-x}Sn_xS_{12}$.[25]

Lithium substructure. Here the lithium substructure is probed from neutron diffraction data to assess changes in the series of solid solutions. The isovalent substitution of P(+V) with Sb(+V) does not change the Li^+ carrier concentration in the structure, hence the amount of Li ions moving through the unit cell remains constant. As discussed above, all the Li ions are distributed over the four lithium sites Li(1), Li(2), Li(3) and Li(4) in the LGPS structure. In the investigated series, the introduction of antimony on the M(1)/P(1) site leads to a slight change of Li^+ occupancy (Figure 5). These co-refinements show that a maximum of 1% of Li ions are shifted between the four Li^+ positions (Figure S4). As these are within the refinement uncertainty, this indicates that the relative site energies of each crystallographic Li^+ site are similar and do not change drastically upon Sb(+V) introduction.

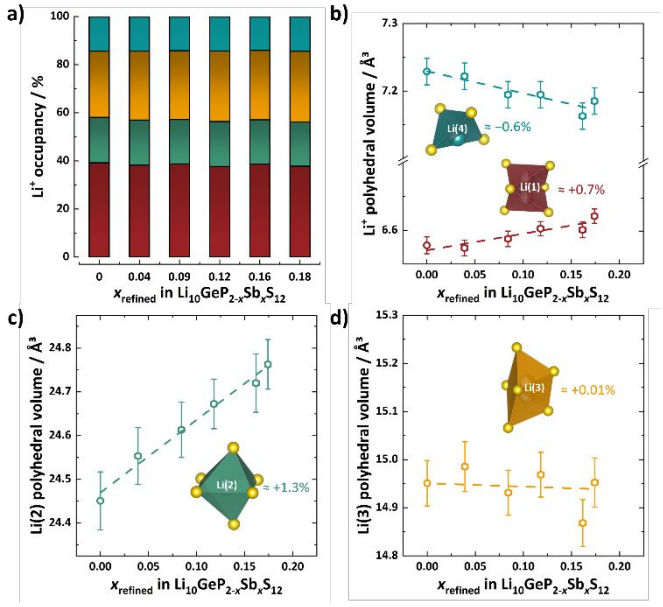

Figure 5: *(a) The lithium occupancies of Li(1) (red), Li(2) (green), Li(3) (orange) and Li(4) (turquoise) do not change antimony content. (b) The Li(1) polyhedral volume increases (+0.7%), while the Li(4) polyhedral volume decreases (−0.6%) with increasing substitution content. (c) The volume of the octahedral Li(2) position increases (+1.3%) with increasing substitution level. (d) The Li(3) polyhedral volume remains fairly constant with increasing Sb content (+0.01%). The dashed lines represent guides-to-the-eye and all structural changes are giving in percentage to gauge the minor overall changes.*

The introduction of antimony into the LGPS structure leads to a slight increase in the polyhedral volume of Li(1) and Li(2), a decrease in the Li(4) polyhedral volume and a somewhat constant Li(3) polyhedral volume (Figure 5b to 5d). The Li(2) octahedron exhibits the most pronounced change in volume with an increase of ≈1.3%. Considering the refinement uncertainties these changes are minor but in agreement with the overall structural changes. For instance, the expansion of Li(2) octahedron is in line with the elongation of the unit cell, the Li(2) octahedron and M(1)/P(1) tetrahedron are directly connected and form chains along the *c*-axis (Figure 1a). Moreover, Li(1) and Li(3) polyhedra form chains along the *c*-direction as well. In contrast to Li(2) octahedron, the Li(1) tetrahedron barely increases only about 0.7% and Li(3) polyhedron only 0.01%, in other words only tiny changes can be seen. Considering the multiplicity, the absolute volume change of the Li(1)-Li(3) chain is 0.71 Å³, while the absolute volume increase of the Li(2)-M(1)/P(1) chain is 1.68 Å³ (Figure S5). The Li(1)-Li(3) polyhedral chain expansion is roughly 43% of the volume increase of the Li(2)-M/P(1) polyhedral chain indicating that the expansion of the latter chain cannot be completely in *c*-direction, since both chains are constricted via the same sulfur atoms (Figure S6b) and a much higher elongation in *c*-direction of one chain would result in a distortion or even disruption of the structure. Looking at S(*X*)-S(*X*) distances within Li(2) octahedron, the S(1)-S(1) distance and S(2)-S(2) increases (Figure S6a and S6c), which is an expansion in the *ab*-plane. The S(2)-S(3) distances of the octahedron is increasing being the evidence for the enlargement in *c*-direction (Figure S6d). Overall, the volume of the Li^+ sublattice is slightly expanding in the *c*-direction and into the *ab*-plane, consistent with the average structural changes. Nevertheless, the changes to the Li^+ – Li^+ distances and Li^+ polyhedra are very minor and the Li^+ distribution remains similar for all compositions in this series of solid solutions.

Ionic transport characterized by impedance spectroscopy. The conductivity of the samples was probed by AC impedance measurements in the temperature range of 233 K – 333 K. Exemplary impedance spectra and fits are shown in Figure 6a. For temperatures above 283 K the blocking behaviour of the gold blocking electrodes and induction, indicated by a positive imaginary impedance in the high frequency range, are observed. These inductances show up as the materials themselves exhibit a high conductivity and low overall resistance. Therefore, the ionic conductivity in this temperature range cannot be reliably extracted. Nevertheless, at lower temperatures the impedance spectra consist of only one process and the blocking behaviour of the Au electrodes. In accordance to the observed features in the impedance spectra, the data are fit either with a resistor in series with a constant-phase element or a parallel resistor - constant-phase element in

series with a constant-phase element. The semicircles in the low temperature data show α-values between 0.85 to 0.92 and capacitances of $7 \cdot 10^{-11}$ F to $8 \cdot 10^{-11}$ F, indicating a single process or superposed processes on similar time scales.[37,43] Liang *et al*. observed suppressed semicircles for temperatures lower than 238 K suggesting two processes, e.g. grain and grain boundary. However, this behaviour cannot be observed here. Nevertheless, as additional processes cannot be ruled out, the reported conductivities represent total conductivities.

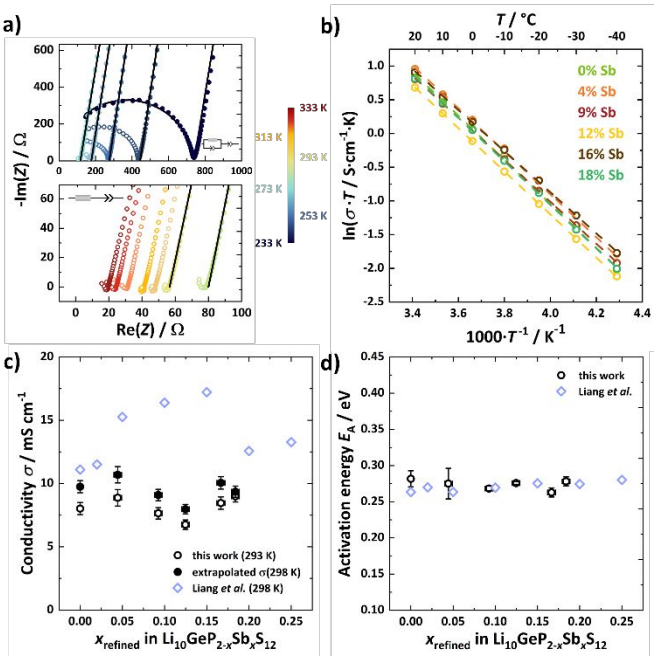

Figure 6: *(a) Exemplary impedance fits for the $Li_{10}GeP_{1.88}Sb_{0.12}S_{12}$ within the temperature range of 233 K to 333 K. The impedance spectra at temperatures higher than 293 K are neglected for the Arrhenius plot due to the occurring inductance at high frequencies. (b) Arrhenius plot for the solid solution series. (c) The conductivity at 20°C and the extrapolated room-temperature conductivity and (d) the activation energy E_A vary within the error interval. For comparison, the conductivity and activation energy values of the nominal compositions by Liang et al. are displayed.[29] The continuous and dashed lines represent fits.*

For the determination of the activation energy all temperatures over 293 K are excluded due to the inductance and with it the overestimation of the resistance, which leads to an underestimation of the ionic conductivity and thereby a change in slope of the Arrhenius fit (Figure S7). A change in slope is often related to a change in diffusion mechanism e.g. due to phase transition. However, as this change is likely from the inductance as well as the fact that there is no change expected within this temperature range as previous reports show,[13,16,27] these data points can be neglected. Within the monitored temperature range, the Arrhenius plot shows linear behaviour (Figure 6b). Despite neglecting 298 K data for determining the activation energy, the Arrhenius data can be used to extrapolate linearly to 298 K.[44] This extrapolated room-temperature conductivity is shown in Figure 6c for comparability to other publications. The determined ionic conductivity and the activation energies stay similar over the substitution series (Figure 6c and 6d). In contrast to Liang *et al*., no increase in conductivity is observed and the highest conductivity value of 17.5 mS·cm^{-1} cannot be reached.[29] For LGPS an extrapolated room-temperature conductivity of 9.8(5) mS·cm^{-1} and an activation energy E_A of 0.28(1) eV can be determined, which is in good agreement with reported literature values.[13,27,29,45] The extrapolated room-temperature conductivities of the substitution series range within 8.0(4) mS·cm^{-1} to 10.7(6) mS·cm^{-1} and the corresponding activation energies E_A are varying between 0.26(1) eV and 0.28(1) eV. All these deviations are within the expected uncertainty for impedance measurements in sulfide solid electrolyte.[44]

Structure-property relationships

The antimony substitution in LGPS seems to mainly cause geometrical changes indicated by (only) slightly altered polyhedral volumes and the elongation in *c*-direction. However, it is puzzling why the ionic conductivity is seemingly not affected by the substitution. For this reason, a structural bottleneck and bond distances are monitored to assess possible counteracting effects or maybe no effects at all.

In line with the thought of an inductive effect, the substitution of P(+V) with Sb(+V) may cause an increase in electron density on the sulfur due to the introduction of the more electropositive element. To probe this, we use the approach of Culver *et al*.[28] that monitored the changes in Li – S distances. In this case, a change in electron density on the sulfur should affect the Li(1)-S(2) and Li(3)-S(2) distances, because S(2) is a corner of the M(1)/P(1) tetrahedron and therefore the Li(*X*)-S(2) distance should be directly influenced by the substituent antimony (Figure 1c and Figure 7a). In order to reliably assess these changes, all data are averaged based on the temperature dependent values as recently performed by Culver *et al.*[28]

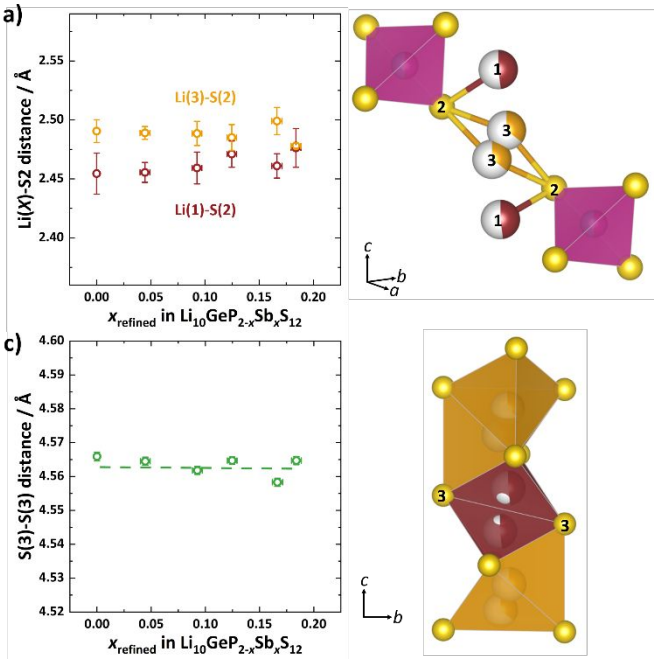

Figure 7: *(a) The temperature-averaged Li(1)-S(2) and Li(3)-S(2) distance do not change. Visualization of structural motif. (b) Also the S(3)-S(3) distance within the Li(1) polyhedron is not changing. Visualization of structural motif. The dashed line is a guide-to-the-eye.*

Theoretically, a decrease in Li - S bond length would be expected for Sb(+V) substituted compositions, since a sulfur with a higher electron density would attract Li^+ stronger (Figure 2). Nevertheless, no significant change in the bond lengths is observed. Similarly, the Raman spectra indicate the presence of Sb(+V) in the structure, however no shift in wavenumber was observed for the polyhedral units. Both observations hint at a low magnitude or even the complete absence of an inductive effect, possibly related to the limited solubility of Sb(+V) in the LGPS structure. One additional drawback may be the presence of germanium on the M(1)/P(1) site showing a similar electronegativity like antimony.[32] Therewith, the overall observable effect is already diminished compared to the $Li_{10}Ge_{1-x}Sn_xS_{12}$ substitution.[28] A proposed bottleneck for Li^+ diffusion is the S(3)-S(3) distance in the Li(1) polyhedron being part of the main diffusion pathway (Figure 7b).[19,27] A shortening of the distance would be detrimental to the conductivity, while a lengthening has a positive impact on ionic motion. However, the S(3)-S(3) distance remains unchanged in this study confirming the observed similar conductivities. Furthermore, an increase in conductivity can be associated with a decrease in Li(1)-Li(1) distance (Figure S8). However, here the Li(1)-Li(1) bond distance also reflects the conductivity trend and shows a comparable distance for all samples. In addition, the temperature-dependence of the Li(1)-Li(1) distance exactly follows the trend showing smaller distances at higher temperatures. Overall, the introduction of Sb(+V) only leads to minor changes of the initial LGPS structure and therefore, the Li^+ ion substructure and motion is barely affected.

Conclusions

The substitution series $Li_{10}GeP_{2-x}Sb_xS_{12}$ ($0 \le x \le 0.25$) was prepared by a mechanochemical synthesis. Antimony replaces phosphorus on the cation disordered site (Wyckoff 4*d*) resulting in a volume increase of $(M/PS_4)^{n-}$ and an elongation of the unit cell along the *c*-direction. An investigation of the Li^+ sublattice shows minor if not negligible changes in Li^+ distribution and disorder and no significant change in any particular bond distances, indicating the absence of strong structural changes or any inductive effect. In line with the minor changes, all compositions in the series exhibit a similar ionic conductivity. This study further emphasizes the importance of correlating structural changes, caused by substitutions, with ionic transport to improve the design concept of solid electrolyte materials and shows that substitutions do not always necessarily affect ionic transport.

Author Contributions

The idea was conceived by B.H. and W.G.Z. The sample preparation and impedance measurements were performed by L.M.G. X-ray diffraction, neutron diffraction, Rietveld refinements, impedance and Raman analysis was carried out by B.H. Neutron diffraction was measured by C.L. All authors discussed the data and data analyses. B.H. and W.G.Z. wrote the manuscript.

Conflicts of interest

There are no conflicts to declare.

Acknowledgements

The research as supported by the Deutsche Forschungsgemeinschaft (DFG) under grant number ZE 1010/13-1. A portion of this research used resources at the Spallation Neutron Source, a DOE Office of Science User Facility operated by the Oak Ridge National Laboratory.

References

1 J. Janek and W. G. Zeier, *Nat. Energy*, 2016, **1**, 16141.
2 Z. Zhang, Y. Shao, B. Lotsch, Y. S. Hu, H. Li, J. Janek, L. F. Nazar, C. W. Nan, J. Maier, M. Armand and L. Chen, *Energy Environ. Sci.*, 2018, **11**, 1945–1976.
3 P. Li, Z. Ma, J. Shi, K. Han, Q. Wan, Y. Liu and X. Qu, *Chem. Rec.*, 2022, e202200086.
4 T. Famprikis, P. Canepa, J. A. Dawson, M. S. Islam and C. Masquelier, *Nat. Mater.*, 2019, **18**, 1278–1291.
5 H.-J. Deiseroth, S.-T. Kong, H. Eckert, J. Vannahme, C. Reiner, T. Zaiß and M. Schlosser, *Angew. Chemie*, 2008, **120**, 767–770.
6 L. Zhou, A. Assoud, Q. Zhang, X. Wu and L. F. Nazar, *J. Am. Chem. Soc.*, 2019, **141**, 19002–19013.
7 M. A. Kraft, S. Ohno, T. Zinkevich, R. Koerver, S. P. Culver, T. Fuchs, A. Senyshyn, S. Indris, B. J. Morgan and W. G.

Zeier, *J. Am. Chem. Soc.*, 2018, **140**, 16330–16339.

8 A. Gautam, M. Ghidiu, A.-L. Hansen, S. Ohno and W. G. Zeier, *Inorg. Chem.*, 2021, **60**, 18975–18980.

9 R. Kanno, T. Hata, Y. Kawamoto and M. Irie, *Solid State Ionics*, 2000, **130**, 97–104.

10 B. T. Leube, K. K. Inglis, E. J. Carrington, P. M. Sharp, J. F. Shin, A. R. Neale, T. D. Manning, M. J. Pitcher, L. J. Hardwick, M. S. Dyer, F. Blanc, J. B. Claridge and M. J. Rosseinsky, Solid State NMR, and Computational Studies, *Chem. Mater.*, 2018, **30**, 7183–7200.

11 N. Minafra, K. Hogrefe, F. Barbon, B. Helm, C. Li, H. M. R. Wilkening and W. G. Zeier, *Chem. Mater.*, 2021, **33**, 727–740.

12 T. Kimura, A. Kato, C. Hotehama, A. Sakuda, A. Hayashi and M. Tatsumisago, *Solid State Ionics*, 2019, **333**, 45–49.

13 N. Kamaya, K. Homma, Y. Yamakawa, M. Hirayama, R. Kanno, M. Yonemura, T. Kamiyama, Y. Kato, S. Hama, K. Kawamoto and A. Mitsui, *Nat. Mater.*, 2011, **10**, 682–686.

14 S. Hori, K. Suzuki, M. Hirayama, Y. Kato, T. Saito, M. Yonemura and R. Kanno, *Faraday Discuss.*, 2014, **176**, 83–94.

15 Y. Kato, S. Hori and R. Kanno, *Adv. Energy Mater.*, 2020, **10**, 1–25.

16 O. Kwon, M. Hirayama, K. Suzuki, Y. Kato, T. Saito, M. Yonemura, T. Kamiyama and R. Kanno, *J. Mater. Chem. A*, 2015, **3**, 438–446.

17 S. Song, S. Hori, Y. Li, K. Suzuki, N. Matsui, M. Hirayama, T. Saito, T. Kamiyama and R. Kanno, *Chem. Mater.*, 2022, **34**, 8237–8247.

18 Y. Wang, W. D. Richards, S. P. Ong, L. J. Miara, J. C. Kim, Y. Mo and G. Ceder, *Nat. Mater.*, 2015, **14**, 1026–1031.

19 M. Inagaki, K. Suzuki, S. Hori, K. Yoshino, N. Matsui, M. Yonemura, M. Hirayama and R. Kanno, *Chem. Mater.*, 2019, **31**, 3485–3490.

20 D. A. Weber, A. Senyshyn, K. S. Weldert, S. Wenzel, W. Zhang, R. Kaiser, S. Berendts, J. Janek and W. G. Zeier, *Chem. Mater.*, 2016, **28**, 5905–5915.

21 S. Hori, R. Kanno, O. Kwon, Y. Kato, T. Yamada, M. Matsuura, M. Yonemura, T. Kamiyama, K. Shibata and Y. Kawakita, *J. Phys. Chem. C*, 2022, **126**, 9518–9527.

22 X. Liang, L. Wang, Y. Jiang, J. Wang, H. Luo, C. Liu and J. Feng, *Chem. Mater.*, 2015, **27**, 5503–5510.

23 R. Iwasaki, S. Hori, R. Kanno, T. Yajima, D. Hirai, Y. Kato and Z. Hiroi, *Chem. Mater.*, 2019, **31**, 3694–3699.

24 J. Gao, X. Sun, C. Wang, Y. Zhang, L. Yang, D. Song, Y. Wu, Z. Yang, T. Ohsaka, F. Matsumotoc and J. Wu, *ChemElectroChem*, 2022, **9**, e202200156.

25 Q. Wang, D. Liu, X. Ma, Q. Liu, X. Zhou and Z. Lei, *J. Colloid Interface Sci.*, 2022, **627**, 1039–1046.

26 Y. Kato, R. Saito, M. Sakano, A. Mitsui, M. Hirayama and R. Kanno, *J. Power Sources*, 2014, **271**, 60–64.

27 T. Krauskopf, S. P. Culver and W. G. Zeier, *Chem. Mater.*, 2018, **30**, 1791–1798.

28 S. P. Culver, A. G. Squires, N. Minafra, C. W. F. Armstrong, T. Krauskopf, F. Böcher, C. Li, B. J. Morgan and W. G. Zeier, *J. Am. Chem. Soc.*, 2020, **142**, 21210–21219.

29 J. Liang, N. Chen, X. Li, X. Li, K. R. Adair, J. Li, C. Wang, C. Yu, M. Norouzi Banis, L. Zhang, S. Zhao, S. Lu, H. Huang, R. Li, Y. Huang and X. Sun, *Chem. Mater.*, 2020, **32**, 2664–2672.

30 R. D. Shannon, *Acta Crystallogr. Sect. A*, 1976, **32**, 751–767.

31 P. Till, M. T. Agne, M. A. Kraft, M. Courty, T. Famprikis, M. Ghidiu, T. Krauskopf, C. Masquelier and W. G. Zeier, *Chem. Mater.*, 2022, **34**, 2410–2421.

32 M. Rahm, T. Zeng and R. Hoffmann, *J. Am. Chem. Soc.*, 2019, **141**, 342–351.

33 A. F. Holleman, E. Wiberg and N. Wiberg, Walter de Gruyter, Berlin, New York, 2007.

34 A. A. Coelho, *TOPAS-Academic*.

35 A. Huq, M. Kirkham, P. F. Peterson, J. P. Hodges, P. S. Whitfield, K. Page, T. Hűgle, E. B. Iverson, A. Parizzi and G. Rennich, *J. Appl. Crystallogr.*, 2019, **52**, 1189–1201.

36 K. Momma and F. Izumi, *J. Appl. Crystallogr.*, 2011, **44**, 1272–1276.

37 G. J. Brug, A. L. G. van den Eeden, M. Sluyters-Rehbach and J. H. Sluyters, *J. Electroanal. Chem. Interfacial Electrochem.*, 1984, **176**, 275–295.

38 S. T. Kong, Ö. Gün, B. Koch, H. J. Deiseroth, H. Eckert and C. Reiner, *Chem. - A Eur. J.*, 2010, **16**, 5138–5147.

39 C. Dietrich, D. A. Weber, S. J. Sedlmaier, S. Indris, S. P. Culver, D. Walter, J. Janek and W. G. Zeier, *J. Mater. Chem. A*, 2017, **5**, 18111–18119.

40 D. Xie, S. Chen, Z. Zhang, J. Ren, L. Yao, L. Wu, X. Yao and X. Xu, *J. Power Sources*, 2018, **389**, 140–147.

41 T. Fuchs, S. P. Culver, P. Till and W. G. Zeier, *ACS Energy Lett.*, 2020, **5**, 146–151.

42 W. Mikenda and A. Preisinger, *Spectrochim. Acta Part A Mol. Spectrosc.*, 1980, **36**, 365–370.

43 J. T. S. Irvine, D. C. Sinclair and A. R. West, *Adv. Mater.*, 1990, **2**, 132–138.

44 S. Ohno, T. Bernges, J. Buchheim, M. Duchardt, A. K. Hatz, M. A. Kraft, H. Kwak, A. L. Santhosha, Z. Liu, N. Minafra, F. Tsuji, A. Sakuda, R. Schlem, S. Xiong, Z. Zhang, P. Adelhelm, H. Chen, A. Hayashi, Y. S. Jung, B. V. Lotsch, B. Roling, N. M. Vargas-Barbosa and W. G. Zeier, *ACS Energy Lett.*, 2020, **5**, 910–915.

45 Y. Sun, K. Suzuki, K. Hara, S. Hori, T. A. Yano, M. Hara, M. Hirayama and R. Kanno, *J. Power Sources*, 2016, **324**, 798–803.